Journal of Materials Chemistry C

ROYAL SOCIETY OF CHEMISTRY

PAPER

View Article Online
View Journal

Cite this: DOI: 10.1039/d5tc04337a

High-performance stretchable thermoelectric multilayers enabled by a synergistic elastomer-conjugated network

Suk Hoon Lim,[a] Mario Culebras,[b] Yong Tae Park,*[c] Jung Sang Cho*[d] and Chungyeon Cho*[ae]

Received 10th December 2025,
Accepted 17th February 2026

DOI: 10.1039/d5tc04337a

rsc.li/materials-c

The development of wearable electronics is critically dependent on the creation of power sources that are not only efficient but also mechanically compliant to withstand the dynamic movements of the human body. This work introduces a novel, water-based layer-by-layer (LbL) assembly of a quadlayer (QL) nanocomposite designed to address this challenge. The architecture comprises an alternating sequence of a high-performance thermoelectric (TE) bilayer (BL), consisting of cationic polypyrrole nanoparticles (PPyNPs) and an anionic dispersion of double-walled carbon nanotubes stabilized with poly(3,4-ethylenedioxythiophene):polystyrene sulfonate (DWNT-PEDOT:PSS), and an elastomeric BL of polyethylene oxide (PEO) and poly(acrylic acid) (PAA). The 20 BL PPyNPs/DWNT-PEDOT:PSS thin films exhibit a high power factor of 183.3 μW m^{-1} K^{-2}, driven by a desirable decoupling of electrical conductivity and Seebeck coefficient, a phenomenon attributed to interfacial energy filtering effects inherent to the nanostructured assembly. Incorporation of elastomeric PEO/PAA layers yields crack-free QL films that sustain up to 30% strain while maintaining ~88% of the initial Seebeck coefficient, with only modest resistance changes. Remarkably, the TE properties decrease by less than 11% after 1000 bending and twisting cycles, underscoring the superior durability of the multilayers.

1 Introduction

The rapid proliferation of wearable and stretchable electronics has initiated a paradigm shift in consumer and medical technology, with applications ranging from health monitoring and smart textiles to soft robotics.[1] However, a primary bottleneck impeding the realization of truly autonomous and ubiquitous wearable systems is the development of conformable, reliable, and maintenance-free power sources.[2] Conventional batteries, while effective, are limited by their rigidity, finite lifetime, and weight, making them ill-suited for seamless integration with the human body or dynamic structures.[3,4] This challenge has spurred intensive research into alternative energy harvesting strategies capable of sustainably converting ambient energy into usable electrical power. Among the available energy harvesting technologies, such as piezoelectric, triboelectric, photovoltaic, and biofuel cells, thermoelectric (TE) generation has emerged as an especially attractive solution for wearable platforms.[5–7] TE devices directly convert thermal gradients into electricity based on the Seebeck effect, offering distinct advantages: they are solid-state (no moving parts), capable of continuous operation, and can exploit the stable temperature gradient between the human body (~36.5 °C) and the ambient environment.[8,9] The efficiency of a TE material is quantified by the dimensionless figure of merit, ZT, defined by the equation: $ZT = \sigma S^2 T \kappa^{-1}$ where S is the Seebeck coefficient, σ is the electrical conductivity, κ is the thermal conductivity, and T is the absolute temperature. A high ZT requires the simultaneous optimization of a large power factor (PF = σS^2) and low κ. Achieving this balance is notoriously difficult due to the interdependence of these parameters; strategies that enhance σ often reduce S, while efforts to suppress κ may inadvertently disrupt electrical pathways.[10,11]

Inorganic semiconductors such as bismuth telluride (Bi_2Te_3) and lead telluride (PbTe) have dominated TE research, achieving ZT values exceeding unity.[12,13] Their crystalline order, high carrier mobilities, and favorable band structures make them

[a] Department of Carbon Convergence Engineering, College of Engineering, Wonkwang University, Iksan, 54538, Republic of Korea. E-mail: cncho37@wku.ac.kr
[b] Institute of Materials Science (ICMUV) Catedrático José Beltrán, 2, Paterna, València 46980, Spain
[c] School of Mechanical Systems Engineering, Myongji University, 116 Myongji-ro, Cheoin-gu, Yongin, Gyeonggi 17058, Republic of Korea. E-mail: ytpark@mju.ac.kr
[d] Department of Engineering Chemistry, Chungbuk National University, Chungbuk, 361-763, Republic of Korea. E-mail: jscho@chungbuk.ac.kr
[e] Department of Biomedical Materials Science, Jeonbuk Advanced Bio-convergence Academy, Wonkwang University, Iksan, Jeonbuk 54538, Republic of Korea

efficient energy converters.[14] However, their applicability to wearable systems is limited: these materials are brittle, heavy, composed of scarce and sometimes toxic elements, and require high-temperature vacuum processing.[15] Their incompatibility with flexible substrates and aqueous, low-cost processing routes presents a fundamental barrier to integration with soft, deformable platforms. In contrast, organic TE materials, particularly conducting polymers such as polypyrrole (PPy), polyaniline, and poly(3,4-ethylenedioxythiophene):polystyrene sulfonate (PEDOT:PSS), have emerged as highly promising alternatives.[16,17] These polymers, often further engineered with carbon-based nanomaterials (graphene, CNT, carbon nanofibers), possess a combination of attributes ideally suited for wearable electronics: low density, intrinsic mechanical compliance, low-temperature solution processability, and abundant, non-toxic elemental composition.[18,19] Their amorphous or semi-crystalline morphology further imparts inherently low κ (≤ 0.5 W m^{-1} K^{-1}), a property critical for achieving favorable ZT values. Over the past decade, remarkable progress has been achieved in enhancing their electronic transport properties through strategies such as secondary doping, post-treatments, and nanoscale structuring.[20–22] As a result, power factors exceeding 1000 μW m^{-1} K^{-2} have been reported for optimized polymer composites, narrowing the gap with their inorganic counterparts.[23–25]

Despite this progress, a persistent challenge remains: simultaneously achieving high TE performance and mechanical stretchability. Wearable electronics must tolerate not only bending and folding but also large-strain deformations ($>20\%$) associated with skin-like or textile integration.[26,27] However, the mechanisms that underpin high σ in polymer nanocomposites, such as dense conductive filler networks, extended π–π stacking, and ordered crystalline domains, are inherently antagonistic to mechanical compliance. Increasing filler content enhances carrier transport but leads to rigidity, brittleness, and strain localization.[28] Conversely, strategies that improve stretchability, such as blending with elastomers or incorporating soft domains, often disrupt percolated conductive pathways and drastically reduce σ and PF.[29,30] This imbalance between electrical performance and mechanical stretchability remains the central bottleneck for realizing practical TE harvesters in wearable form factors.

Addressing this dilemma requires moving beyond conventional bulk blending and toward more sophisticated nanoscale structural engineering. Among various fabrication strategies, layer-by-layer (LbL) self-assembly stands out as an exceptionally versatile bottom-up approach. Based on sequential adsorption of oppositely charged species, the LbL method enables the construction of nanostructured multilayers with sub-nanometer precision in thickness, composition, and architecture.[31,32] It offers unparalleled flexibility in combining diverse classes of materials, such as conducting polymers, nanoparticles, carbon nanomaterials, and elastomers into hybrid films with controlled hierarchical organization. In recent years, LbL films have been successfully engineered for applications ranging from flame retardant coatings and barrier films to drug delivery and biosensing.[33–36] Its potential for wearable TE materials, however, remains largely untapped.

In this work, we report the rational design of high-performance, stretchable TE composites *via* LbL assembly of complementary functional layers. We constructed a synergistic multilayered architecture in which electronically conductive layers are alternated with elastomeric, ductile layers at the nanoscale. Specifically, the TE bilayer (BL) comprises cationic PPy nanoparticles (PPyNPs) electrostatically paired with double-walled carbon nanotubes (DWNT) dispersed in anionic PEDOT:PSS solutions. This conductive BL was designed to maximize the PF through multidimensional charge transport pathways combining conjugated polymers and CNT networks. The trade-off between thermoelectric efficiency and mechanical stretchability has been systematically discussed in a recent review, which highlights that improved compliance often disrupts conductive percolation while high-PF architectures are frequently mechanically rigid.[37] Guided by this perspective, our LbL design uses nanoscale alternation of a rigid conductive bilayer and a hydrogen-bonded elastomer bilayer to maintain charge-transport functionality while enabling large-strain deformability. The elastomeric BL consists of hydrogen-bonded polyethylene oxide (PEO) and poly(acrylic acid) (PAA), known for their exceptional ductility and ability to sustain large tensile strains. By alternating these two distinct BL, we engineered a hierarchical nanostructure in which rigid, conductive networks are mechanically buffered by compliant elastomeric spacers. This architectural design simultaneously preserves high carrier transport efficiency and dissipates mechanical strain, thereby addressing the long-recognized challenge of balancing conductivity with stretchability. The resulting films exhibit robust TE properties under repeated large-strain deformations, demonstrating both high PF and excellent mechanical durability. While several LbL-assembled organic thermoelectric films have achieved exceptionally high power factors (>2000 μW m^{-1} K^{-2}) through densely packed electrostatic conjugated networks, these systems are generally mechanically rigid and lack stretchability.[24] In contrast, the present work focuses on achieving a balanced integration of thermoelectric performance and mechanical compliance by incorporating hydrogen-bonded elastomer interlayers, enabling stable energy conversion under mechanical deformation.

2. Experimental methods

2.1. Materials and methods

PPyNPs were synthesized *via* chemical oxidative polymerization in a mini-emulsion, as reported in a previous study.[38] Briefly, pyrrole monomer was dispersed in an aqueous Poly(diallyldimethylammonium chloride) solution under ultrasonication to form a mini-emulsion, followed by the addition of Fe-Tos oxidant and H_2O_2 to initiate polymerization. The obtained NPs were purified by repeated centrifugation and redispersed in D.I water. PAA (Mw = 100 000 g mol^{-1}, Sigma-Aldrich, USA) and PEO (Mw = 4 000 000 g mol^{-1}, Polysciences, USA) were used

as received without further purification. DWNT (diameter ~2 nm, length ~1 μm, XB type, Continental Carbon Nanotechnologies, USA) were dispersed in aqueous PEDOT:PSS (Clevios PH1000, Heraeus, Germany) at 2 wt% concentration to ensure colloidal stabilization and prevent aggregation. The dispersion procedure consisted of 30 min of bath sonication, followed by 20 min of probe sonication at 15 W in an ice bath, and an additional 30 min of bath sonication. The resulting stable black suspension was centrifuged at 4000 rpm for 20 min, and the supernatant was collected to eliminate any large bundles or aggregates. All chemicals were used as received without any further purification unless otherwise stated.

2.2. Substrates

Single-side-polished silicon wafers with a thickness of 500 μm (University Wafer, USA) were used as deposition substrates for profilometry, atomic force microscopy (AFM), scanning electron microscopy (SEM), ultraviolet photoelectron spectroscopy (UPS), and nanoindentation. Poly(ethylene terephthalate) (PET) films with a thickness of 179 μm (ST505, DuPont-Teijin Films) were served as flexible substrates for TE measurements. Polyurethane (PU) rubber sheets (0.7 mm thick, WooJin Package, Korea) were selected for mechanical stretchability tests due to their high elasticity and surface compatibility. All substrates were rinsed with methanol and D.I water, and then dried under a nitrogen stream. PET substrates were subjected to corona treatment (BD-20C, Electro-Technic Products, USA), while PU substrates were treated with mild oxygen plasma (Diener ATTO Plasma Cleaner, Germany, 25 W, 5 min) to improve hydrophilicity and promote adhesion of the deposited layers. Polished Ti/Au crystals with a resonance frequency of 5 MHz were purchased from Maxtek, Inc. (Cypress, CA), and used to characterize deposited mass per layer with a quartz crystal microbalance (QCM). After each deposition, the crystal was rinsed and dried and then left on the microbalance to stabilize for 5 min, which minimizes water's contribution to the weight.

2.3. Assembly of multilayer films

The TE multilayers were carried out by an LbL dipping method using a programmable robotic deposition system. For PPyNPs/DWNT-PEDOT:PSS BL films, the substrates were first immersed in positively charged PPyNPs dispersion for 5 min, rinsed thoroughly with D.I water, and subsequently immersed in DWNT-PEDOT:PSS dispersion for 5 min, followed by another rinsing step. This sequence was repeated to build the desired number of BL. The first deposition cycle was performed with a 5 min adsorption time, while subsequent cycles employed a 1 min immersion time. For the preparation of PPyNPs/DWNT-PEDOT:PSS/PEO/PAA QL films, each deposition cycle was carried out in four sequential adsorption steps. The substrates were first immersed in the PPyNPs dispersion, rinsed with D.I water, and then transferred into the DWNT-PEDOT:PSS solution followed by rinsing. Subsequently, the substrates were immersed in the PEO solution, rinsed, and finally deposited with PAA, with a final rinsing step completing one QL cycle. During the initial cycle, the immersion time for each step was set to 5 min, while in subsequent cycles it was reduced to 1 min. The pH of all solutions was maintained at 2.5, a condition under which PEO and PAA undergo strong hydrogen bonding, enabling the formation of elastomeric properties. After deposition, all films were air-dried overnight and subsequently stored in a desiccator to remove residual moisture before characterization.

2.4. Characterization of thin films

The thickness of the multilayer films was monitored using a stylus profilometer (NanoMap-PS, AEP Technology, USA). Each value was averaged from at least 10 independent scans across different regions of the film to ensure reproducibility. The mass of each deposition cycle was measured using a QCM (Inficon, USA) equipped with a 5 MHz Au-coated quartz crystal. Surface morphology was analysed by non-contact mode AFM (Nanostation II, Surface Imaging Systems, Germany) at a scan rate of 0.5 Hz under ambient conditions, and by field-emission SEM (Hitachi S-4800, Japan, Core Facility for Supporting Analysis & Imaging of Biomedical Materials at Wonkwang University supported by the National Research Facilities and Equipment Center by the Korea Basic Science, NFEC-2008-09-066891) operated at 5 kV. The elastic modulus of the films was determined by AFM nanoindentation using the Hertz contact model for force–displacement curves. To assess the ζ-potential of the PPyNPs in solution, a nanoparticle size analyzer (Zetasizer Nano ZS90, Malvern Instruments Ltd., Worcestershire, U.K.) with a 633 nm laser at a scattering angle of 13°, was used. UV-vis spectroscopy of the thin films deposited on quartz slides was performed using a spectrophotometer (UV-1900, Shimadzu Corporation, Tokyo, Japan).

A four point probe method (CMT-100S®, AIT Co., Ltd., Suwon, Korea) was used to measure the sheet resistance (R_s) of the prepared LbL films (15 mm × 30 mm). This apparatus was equipped with 0.4 mm probe tip diameter and probe spacing of 0.72 mm between tips. Electrical conductivity (σ) was then calculated using $\sigma = (R_s \cdot t)$, where t is the film thickness obtained from a profilometer. The Seebeck coefficient (S) was measured by imposing a controlled temperature gradient (−5 to +5 K) across the film and recording the thermovoltage with a LabVIEW-controlled setup using T-type thermocouples. Prior to measurements, a silver paste was applied to the samples to avoid the electrical contact resistance. The reported S was obtained from the linear slope of ΔT *vs.* ΔV relation. The σ and S values reported represent an average of 5 measurements on 3 independent samples. The power factor was calculated at room temperature. The reported σ and S are the average values of five measurements on three independent samples. Carrier concentration (n) and mobility (μ) were evaluated by Hall effect measurements in van der Pauw geometry (Lake Shore, USA), using magnetic fields up to 0.5 T. Strain-dependent electrical measurements were performed by stretching the films deposited on PU substrates at a strain rate of 0.4 cm s^{-1}, up to 100% elongation, with 1 mm tip spacing. Seebeck voltage was recorded under constant strain. Bending and twisting durability tests were carried out for 1000 cycles. UPS (Sigma Probe, Thermo VG Scientific, UK) was employed to

determine the HOMO energy levels and work functions of the multilayers, enabling correlation between electronic structure and TE properties.

3 Results and discussion

3.1 Controlled film growth and nanostructure formation

Fig. 1 illustrates the LbL deposition process for constructing PPyNPs/DWNT-PEDOT:PSS BL assemblies. This method enables the controlled growth of multilayered thin films by sequentially adsorbing oppositely charged species onto a substrate. The corresponding chemical structures of the polymeric and carbon-based nanomaterials involved in this assembly are also depicted. Detailed experimental conditions, including the solution concentrations, coating parameters, and deposition environment, are described in the Experimental section. The LbL deposition of PPyNPs/DWNT-PEDOT:PSS BL was based on the alternating adsorption of positively charged PPyNPs and negatively charged DWNT-PEDOT:PSS solutions. The synthesized PPyNPs exhibited a ζ-potential value of 27.1 $\pm$ 0.5 mV when measured using dynamic light scattering; this indicates that these NPs carry a positive charge in an aqueous solution. The integration of DWNT within the PEDOT:PSS solution enhances the colloidal stability of the dispersion, facilitating a uniform film formation during each deposition cycle. The electrostatic interactions between cationic PPyNPs and anionic DWNT-PEDOT:PSS are the primary driving force governing the sequential adsorption, ensuring reproducible layer growth with controlled thickness and homogeneity. Homogeneous black dispersions of PPyNPs in water and DWNT suspensions in aqueous PEDOT:PSS are shown in Fig. S1. PPyNPs have a spherical shape, with diameters ranging from 140 to 180 nm, as evidenced by the AFM and SEM images. A photo-image of DWNT in PEDOT:PSS solution highlights the stability of these colloidal dispersions after sonication and centrifugation, indicating that the presence of PEDOT:PSS prevents significant aggregation of the DWNT, a phenomenon that has been reported in previous studies utilizing CNT-based hybrid systems for LbL assembly.[39–41] Both AFM and SEM images of drop-cast dilute solutions on Si-wafers further revealed the homogeneous distribution of DWNT in PEDOT:PSS, with minimal aggregation. This suggests that the incorporation of PEDOT:PSS as a stabilizing agent effectively mitigates the intrinsic van der Waals forces between nanotubes, facilitating their integration into the multilayered architecture.

The fabrication of high-performance TE films *via* LbL assembly depends on the ability to achieve uniform deposition with each cycle. The growth of the PPyNPs/DWNT-PEDOT:PSS BL system was monitored by profilometry and QCM. As shown in Fig. 2a, the film thickness increased linearly with the number of deposited cycles. This linear growth is a characteristic feature of a well-controlled LbL process, demonstrating that each deposition cycle yields a uniform and reproducible contribution to the overall film thickness. Such consistent growth is governed by the strong electrostatic interactions between the positively charged PPyNPs and the negatively charged DWNT-PEDOT:PSS, which ensures controlled adsorption during each deposition step. Additionally, strong π–π interactions among PPyNPs, DWNT, and PEDOT:PSS may contribute to the assembly and networking of the multilayer composites. The PPyNPs/PEDOT:PSS composites also showed a linear growth behavior with less amount of materials deposited (Fig. S2a). PPyNPs/DWNT-PEDOT:PSS grew thicker than the multilayers with no DWNT deposited, which is due to three-dimensional (3D) structure of the nanotubes. The mass increment, as measured by using a QCM, showed similar behavior to the thickness growth of both PPyNPs/PEDOT:PSS and PPyNPs/DWNT-PEDOT:PSS films (Fig. 2b and Fig. S2b). This indicates that the composition remained constant throughout the assembly process. This linear growth has been reported by other studies on LbL-based composites, wherein polyelectrolytes were incorporated with CNT.[42,43] Although the mass increase of the multilayers has only been measured over 10 cycles, it is expected to increase linearly up to 24 cycles, given the steadily increasing thickness observed. With knowledge of both film thickness and mass, the density of PPyNPs/PEDOT:PSS and PPyNPs/DWNT-PEDOT:PSS multilayers was calculated to be $\sim$1.85 and 2.11 g cm^{-3}, respectively. The higher density of the DWNT-based thin film is likely due to a more tightly packed nanostructure.

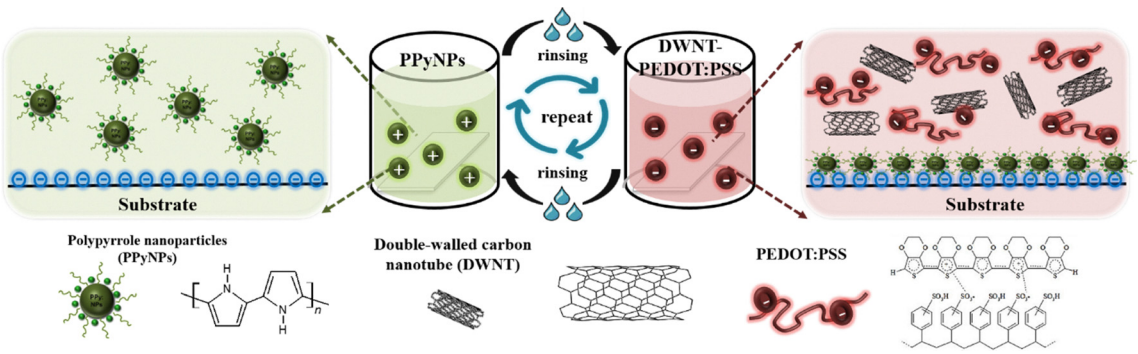

Fig. 1 Schematic illustration of the layer-by-layer (LbL) assembly process of PPyNPs/DWNT-PEDOT:PSS on a substrate, along with chemical structures used in this study. Positively charged PPyNPs and negatively charged DWNT-PEDOT:PSS suspensions are alternately deposited with rinsing steps, yielding a multilayered composite film.

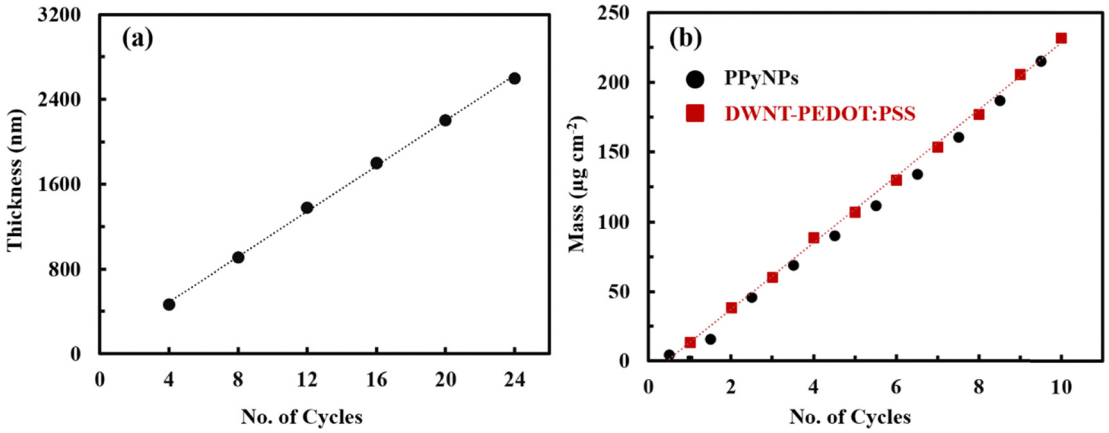

Fig. 2 (a) Thickness evolution of PPyNPs/DWNT-PEDOT:PSS multilayers as a function of bilayer number, measured by profilometry, showing linear growth during LbL assembly. (b) QCM-determined mass increment per unit area for PPyNPs (black circles) and DWNT-PEDOT:PSS (red squares), both exhibiting linear increases, with the DWNT-containing films yielding higher overall growth due to the nanotube framework.

3.2. Surface structure

Morphological surface characterization of the LbL thin films was carried out using AFM and SEM, as shown in Fig. 3. The AFM image of a 10 × 10 μm^2 scanned area (Fig. 3a) revealed that, after deposition of a single bilayer (1 BL), randomly oriented DWNT are uniformly distributed across the film surface. Spherical PPyNPs are homogeneously dispersed and preferentially anchored along DWNT bundles, forming nanoscale junctions. The brighter protrusions are attributed to locally accumulated PPyNPs and PEDOT:PSS domains rather than nanotube aggregation during deposition. Height profile analysis (Fig. 3b) indicates that DWNT exhibit an average thickness of 3–5 nm, while PPyNPs show an average height of ~150 nm, confirming that the nanotubes remain well-exfoliated in the PEDOT:PSS matrix and are uniformly incorporated during LbL assembly. With increasing bilayer number, as in the 5 BL films (Fig. 3c), the surface developed into a more densely entangled network, with enhanced interconnections among PPyNPs, DWNT, and PEDOT:PSS, indicative of the progressive formation of a conjugated 3D nanostructure.

The uniform dispersion and structural development were further corroborated by SEM observations. At 1 BL, the SEM

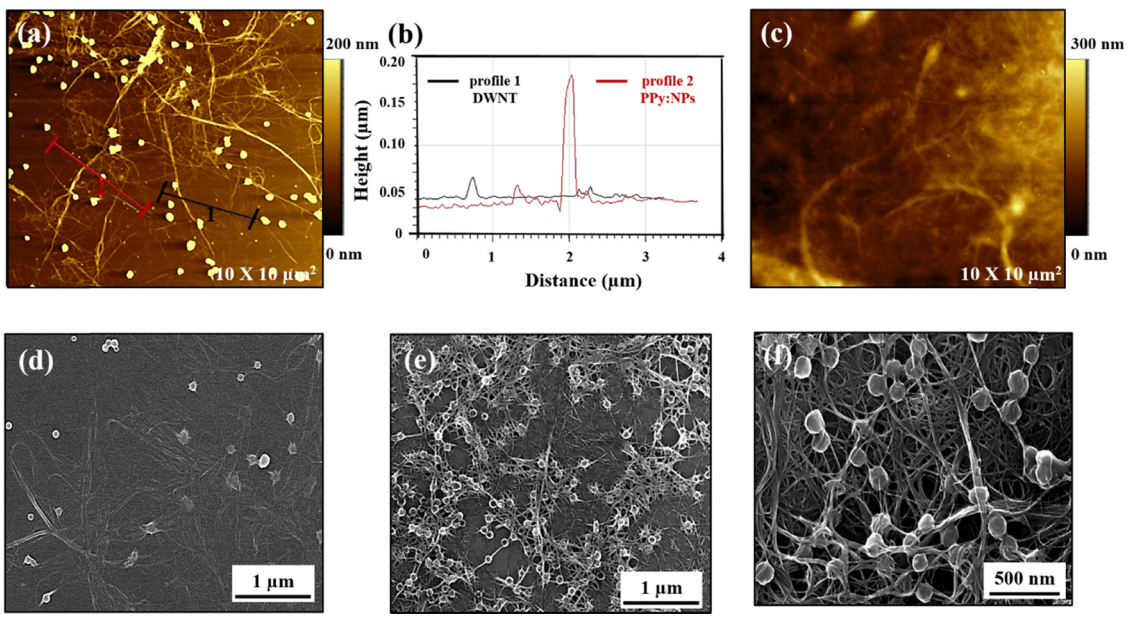

Fig. 3 (a) AFM height image and (b) corresponding height profiles of DWNT (profile 1, black) and PPyNPs (profile 2, red). The black bar (1) and red bar (2) in (a) indicate the line scan positions used for the profiles shown in (b). (c) AFM image of 5 BL PPyNPs/DWNT-PEDOT:PSS films, revealing a more densely packed and uniform surface. Top-view SEM images of (d) 1 BL and (e) 5 BL PPyNPs/DWNT-PEDOT:PSS films show that with increasing bilayer number, the films develop from sparsely distributed structures into a more compact and interconnected nanostructure, where PPyNPs are more extensively conjugated along the entangled DWNT-PEDOT:PSS network. (f) High-magnification SEM image of the 5 BL film highlighting the nanoscale arrangement of DWNT bundles and uniformly anchored PPyNPs, clearly visualizing the conjugated network architecture.

image (Fig. 3d) showed that DWNT serve as conductive bridges, connecting neighboring PPyNPs into an emerging percolation pathway. After five deposition cycles, the surface coverage significantly increased, resulting in an extensively interconnected network of nanotubes and nanoparticles (Fig. 3e). The nanotubes appeared randomly interwoven without preferential alignment, forming a densely entangled architecture with high junction density. A high-magnification SEM image (Fig. 3f) provides deeper insight into the nanoscale organization, highlighting the coexistence of individual PPyNPs and a well-defined DWNT network. The PEDOT:PSS-assisted dispersion ensures uniform nanotube distribution and intimate contact with PPyNPs, thereby constructing a robust conjugated multilayer structure. Such nanoscale interconnectivity is expected to establish efficient electron transport channels, leading to enhanced σ and improved TE performance.

3.3. Thermoelectric properties

To elucidate the electrical transport properties of the multilayer assemblies, the sheet resistance of PPyNPs/PEDOT:PSS and PPyNPs/DWNT-PEDOT:PSS thin films deposited on PET substrates was measured using a four-point probe as a function of the number of BL. For the PPyNPs/PEDOT:PSS system, the sheet resistance decreased progressively with increasing film thickness, leading to σ of 1.43×10^{-2} S cm^{-1} at 20 BL (Fig. S3a). In contrast, incorporation of DWNT induced a dramatic improvement in the electrical properties, with sheet resistance decreasing sharply from 1300 Ω sq^{-1} at 4 BL to 30 Ω sq^{-1} at 20 BL (Fig. 4a). The corresponding conductivity increased nearly tenfold, from 16.7 S cm^{-1} at 4 BL to 151.5 S cm^{-1} at 20 BL, before reaching a plateau beyond 20 BL (147.9 S cm^{-1} at 24 BL). The saturation behavior indicates that electrical transport is governed primarily by the structural connectivity of the multilayered network rather than the simple accumulation of conductive material, underscoring the importance of 3D percolation pathways formed by nanotubes and conductive polymers.[44]

S was also investigated as a function of the number of cycles deposited (Fig. 4b and Fig. S3b). Both films exhibited positive S values, confirming hole-dominated p-type conduction. PPyNPs/PEDOT:PSS multilayers showed a modest increase, reaching 38 μV K^{-1} at 20 BL, corresponding to a relatively low PF of 2.1×10^{-3} μW m^{-1} K^{-2}. In contrast, the PPyNPs/DWNT-PEDOT:PSS assemblies displayed a steady rise in S with increasing thickness, achieving 110 μV K^{-1} at 20 BL. When combined with the enhanced conductivity, these values resulted in a marked increase in PF, reaching 183.3 μW m^{-1} K^{-2} at 20 BL for a film thickness of ~2.2 μm. The synergistic role of DWNT is thus evident, simultaneously improving both charge carrier transport and energy filtering at the PPyNPs-DWNT interfaces, which together enable efficient TE performance in the multilayer system. Beyond 20 BL, both σ and S showed a plateau or slight decrease, indicating that the conductive network approaches structural saturation and that further deposition does not significantly enhance TE performance.

It is particularly noteworthy that the LbL-driven PPyNPs/DWNT-PEDOT:PSS multilayer films exhibited a concurrent increase in both σ and S with the number layers. Such simultaneous enhancement of the two interdependent TE parameters is rarely observed in conventional inorganic TE materials, where σ and S are typically inversely correlated due to the intrinsic constraints imposed by carrier concentration.[45,46] To further clarify this unusual decoupling behavior, Hall effect measurements were conducted using a van der Pauw configuration to determine the carrier concentration (n) and carrier mobility (μ). The reported values represent the average of three independently prepared samples. Based on the relation of ($\sigma = ne\mu$, where e is the elementary charge), a slight decrease in carrier concentration was observed with increasing layers (8.82×1020 cm^{-3} at 12 BL to 7.2×1020 cm^{-3} at 20 BL) (Fig. 5a). However, the μ of 20 BL PPyNPs/DWNT-PEDOT:PSS thin films was calculated to be 1.24 cm^2 V^{-1} s^{-1}, which is more than 3 times larger relative to that (0.38 cm^2 V^{-1} s^{-1}) of the multilayers made at 12 BL. These results suggest that the construction of a highly interconnected 3D conjugated network within the LbL multilayers facilitates more efficient charge transport pathways and suppresses carrier scattering, thereby boosting both σ and S simultaneously. Such morphology-driven

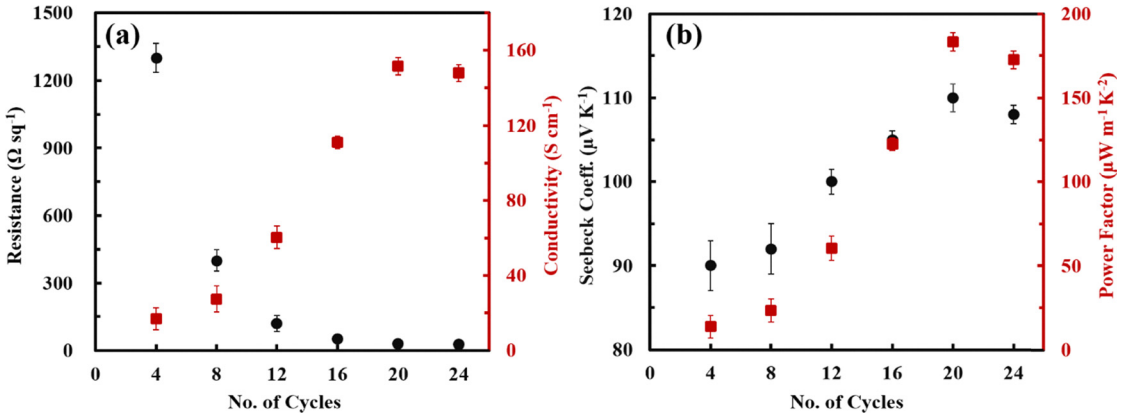

Fig. 4 (a) Sheet resistance (circle) and electrical conductivity (square) and (b) Seebeck coefficient (circle) and power factor (square) of PPyNPs/DWNT-PEDOT:PSS LbL thin films deposited on PET substrates as a function of the number of deposition cycles.

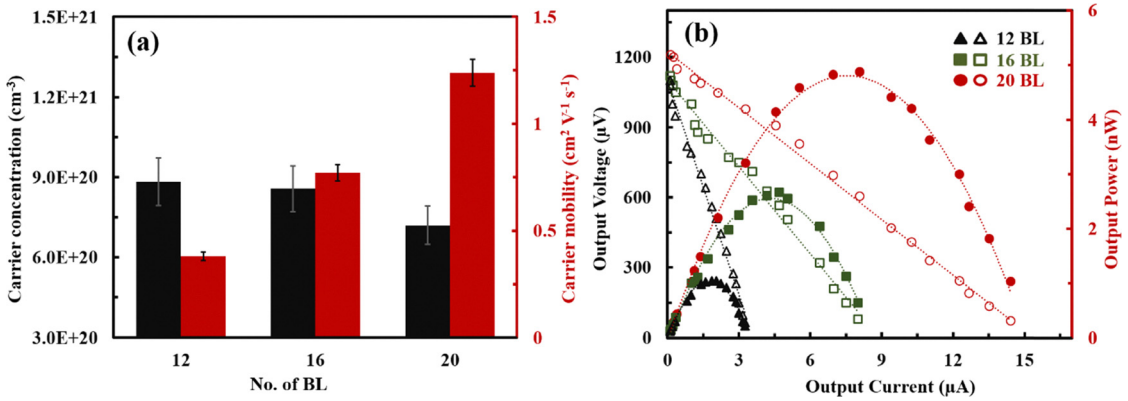

Fig. 5 (a) Carrier concentration and carrier mobility of the PPyNPs/DWNT-PEDOT:PSS films from Hall effect measurements. (b) Output voltage (open symbols) and output power (closed symbols) of the PPyNPs/DWNT-PEDOT:PSS films as a function of bilayers deposited at a temperature difference of 11 K.

improvement in μ represents the key origin of the enhanced PF, highlighting the crucial role of nanoscale structural ordering achieved *via* the LbL assembly process.

To evaluate the TE performance of the multilayer composites under realistic conditions, output voltage and power characteristics were measured for PPyNPs/DWNT-PEDOT:PSS films (2×4 cm^2) subjected to a temperature gradient (ΔT = 11 K) at room temperature (Fig. 5b). When an external load (R_L) is equal to the internal resistance (R_i), the maximum output power should be obtained, which is expressed as $P_{max} = V_{oc}{}^2 4R_i{}^{-1}$ (V_{oc} – open-circuit voltage). The V_{oc} increased systematically from 1100 μV at 12 BL to 1210 μV at 20 BL, confirming enhanced *S*-driven voltage generation with increasing BL number. From the current-power curves, the output power ($P = I{\cdot}V$) exhibited a parabolic dependence on the load resistance, achieving maximum power of 4.88 nW for the 20 BL films. These results indicate that both V_{oc} and P_{max} scale positively with film thickness, reflecting the progressive improvement in the PF of the multilayer system and demonstrating the feasibility of flexible TE energy harvesting using polymer/carbon hybrid architectures. Although the present power output remains below the threshold required for direct application in practical devices, the demonstrated energy harvesting behavior verifies the feasibility of employing these flexible multilayer composites in TE systems. With further refinement of device architecture, such as reducing interfacial contact resistance, optimizing module configuration, and enhancing heat-electric coupling, the overall energy conversion efficiency is expected to improve substantially, enabling future integration into self-powered, flexible, or wearable electronic platforms.

3.4. Highly tunable thermoelectric behavior

The superior TE performance of the PPyNPs/DWNT-PEDOT:PSS multilayered composites can be attributed to a synergistic interplay of three key factors: (i) strengthened intermolecular π–π interactions, (ii) the formation of a three-dimensionally interconnected conjugated network, and (iii) nanoscale interfacial energy filtering effects inherent to the multilayered structure. The UV-vis spectra provide direct evidence of interfacial electronic interactions. As shown in Fig. 6a, pristine PPyNPs and PEDOT:PSS displayed absorption bands centered at ~223 nm and ~225 nm, respectively, originating from π–π* electronic transitions of aromatic rings.[38,47] Upon integration into the PPyNPs/DWNT-PEDOT:PSS multilayers, the main absorption band red-shifted to ~277 nm, signifying an extended conjugation length and strengthened π–π stacking among PPyNPs, PEDOT:PSS, and DWNT. Such a red-shift reflects enhanced orbital overlap at the polymer-nanotube interfaces, facilitating more delocalized charge carriers and thus improving μ. The electronic structure was further examined using UPS. With increasing BL number, the HOMO onset gradually shifted from 4.34 eV at 12 BL to 4.56 eV at 20 BL (Table S1). More notably, the work function (Φ) increased more substantially, from 3.25 eV to 3.88 eV at 12 BL and 20 BL, respectively. As a result, the energy difference $\Delta(E_{HOMO} - \Phi)$ decreased from 1.09 eV at 12 BL to 0.68 eV at 20 BL, indicating that the Fermi level (E_F) progressively approaches the HOMO edge as more layers are deposited. Such movement of E_F toward the valence-band maximum strengthens the p-type character of the films and reduces the energetic barrier for hole transport.[48] More importantly, the evolution of the UPS valence-band slope provides quantitative insight into the Seebeck enhancement. As shown in Fig. 6b, the spectral intensity near E_F became progressively steeper from 12 to 20 BL. According to the Mott relation, $S \propto [\mathrm{d} \ln \sigma(E)/\mathrm{d}E]_{E=E_F}$, an increased slope in the UPS valence region directly reflects a larger density-of-states (DOS) gradient at E_F, which enhances S.[49,50] The consistent correlation between the steeper UPS profile, reduced $\Delta(E_{HOMO} - \Phi)$, and increased S confirms that the electronic structure of the multilayers shifts toward an energetically favorable regime for thermopower generation.

The sequential LbL assembly yields a highly ordered multilayer architecture where PEDOT:PSS-wrapped DWNT act as conductive bridges linking adjacent PPyNPs across neighboring layers, as depicted schematically in Fig. 6c. Under a temperature gradient, these interfaces serve as effective energy-filtering

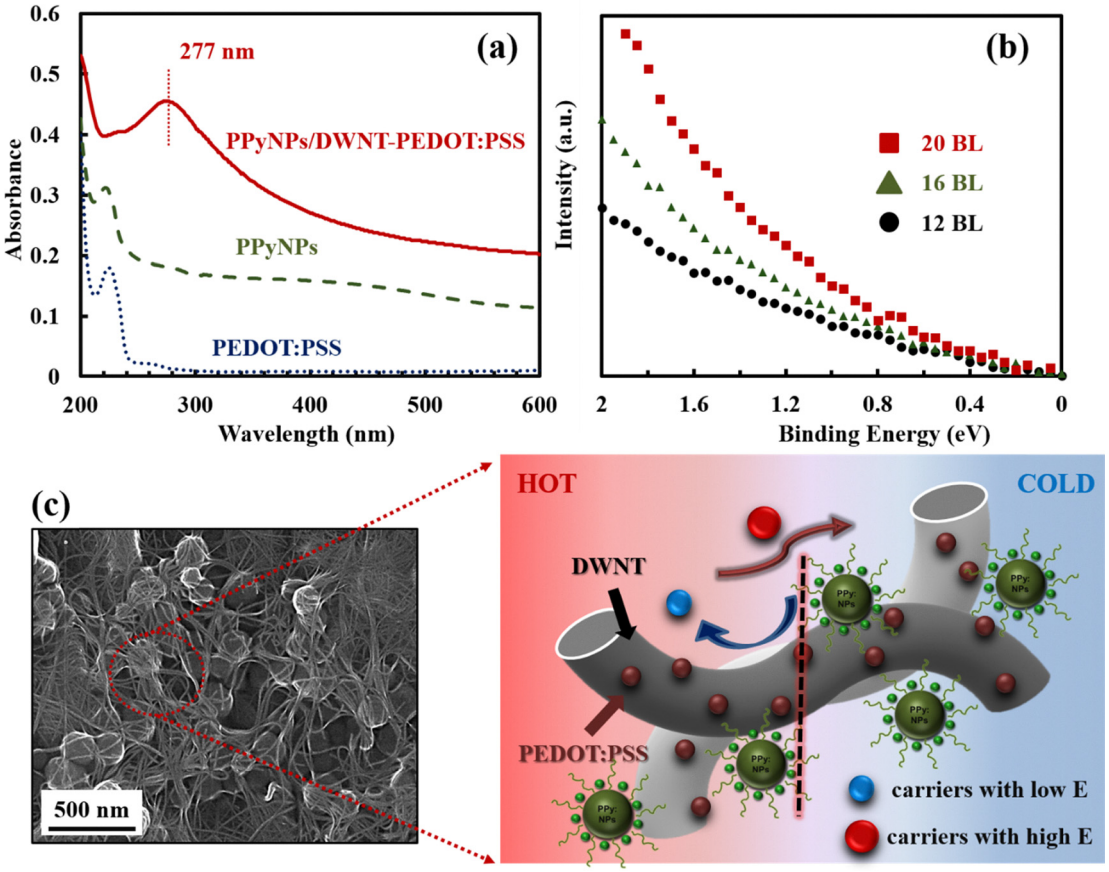

Fig. 6 (a) UV-vis spectra of the aqueous PPyNPs and PEDOT:PSS and 2 BL PPyNPs/DWNT-PEDOT:PSS film and (b) UPS spectra of the PPyNPs/DWNT-PEDOT:PSS films with the number of the layers deposited. (c) Schematic illustration of the carrier transport mechanism within the multilayer structure. The 3D conjugated network formed by PPyNPs, PEDOT:PSS, and DWNT provides efficient transport pathways, while abundant nanoscale interfaces introduce energy filtering effects that selectively transmit high-energy carriers, enabling the simultaneous enhancement of conductivity and Seebeck coefficient.

barriers. Low-energy carriers are preferentially scattered, whereas high-energy carriers can cross the interfacial potential steps, thereby raising the average carrier energy and increasing S without significantly compromising σ.[51,52] This trend is consistent with Hall-effect measurements, which show a modest reduction in n accompanied by an increase μ as more layers are deposited. The combined influence of (i) enhanced π–π interaction-driven mobility increases, (ii) E_F shifting into a region with sharper DOS curvature as revealed by UPS, and (iii) interfacial energy filtering across numerous polymer-carbon junctions, explains the unusual yet highly desirable simultaneous increase in both σ and S. Ultimately, these cooperative mechanisms yield a significantly improved PF, demonstrating that nanoscale structural control through LbL assembly provides an effective route for engineering high-performance TE multilayers.

3.5. Influence of strain on morphological integrity and mechanical properties

While the PPyNPs/DWNT-PEDOT:PSS BL films demonstrate excellent TE properties, their inherent rigidity and susceptibility to cracking under small deformations render them unsuitable for wearable applications. To overcome this limitation, a QL system was rationally designed by interleaving the conductive PPyNPs/DWNT-PEDOT:PSS BL with elastomeric PEO/PAA bilayers (Fig. S4). The QL architecture exhibited linear thickness growth (up to ~2.5 μm for 20 QL cycles) in sharp contrast to the exponential growth behavior of pure PEO/PAA films (Fig. S5). Exponential growth in PEO/PAA systems arises from an "in-and-out" diffusion mechanism, where highly mobile polymer chains from the solution can diffuse into the existing film and intermix.[53,54] The observed transition from exponential to linear growth in the QL system suggests that the dense, non-interpenetrating PPyNPs/DWNT-PEDOT:PSS layers effectively serve as diffusion barriers, thereby restricting the interpenetration of PEO and PAA chains.

The surface structure of the QL architecture was evaluated by depositing films onto a stretchable PU substrate and visualizing their morphology under tensile strain using SEM. As a baseline, SEM images of the PEO/PAA system alone (Fig. S6) revealed a featureless and smooth surface, characteristic of a soft elastomeric film. When PEO/PAA layers were integrated into the QL assembly, the overall morphology of the PPyNPs/DWNT-PEDOT:PSS network was preserved, as confirmed by

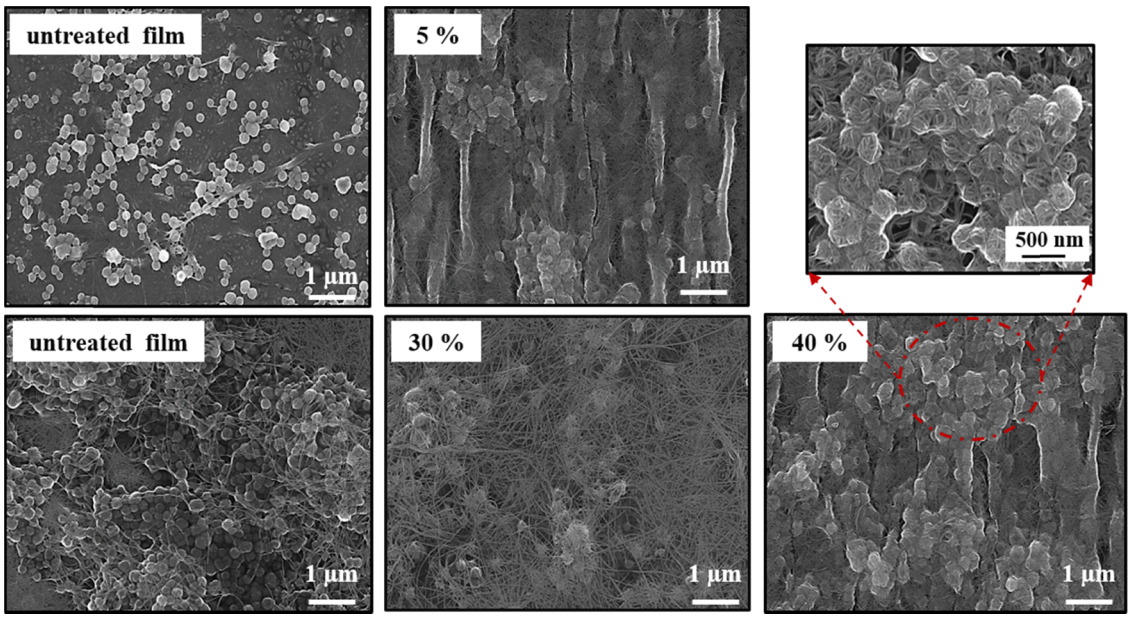

Fig. 7 SEM images of PPyNPs/DWNT-PEDOT:PSS BL (top row) and PPyNPs/DWNT-PEDOT:PSS/PEO/PAA QL (bottom row) films under tensile strain. BL films fractured at ~5% strain, while QL films maintained structural integrity up to 30% strain. At 40% strain, cracks appeared, but the conjugated network remained locally visible.

AFM and SEM analyses (Fig. S7), indicating that the introduction of elastomeric spacers did not disrupt the underlying conjugated nanostructure. The strain-dependent SEM observations further underscore the mechanical benefits of the QL design, as shown in Fig. 7. The control BL films, consisting solely of PPyNPs/DWNT-PEDOT:PSS, fractured catastrophically even under a small elongation of 5%, displaying large surface cracks across the film. In contrast, the QL films exhibited remarkable structural integrity under tensile deformation. The conjugated carbon network remained intact and free of cracks up to 30% strain, highlighting the ability of the PEO/PAA layers to buffer and redistribute stress within the multilayered composite. At 40% strain, initial cracks became visible; however, high-magnification SEM images revealed that the conjugated PEDOT:PSS-CNT-PPyNPs framework persisted locally within the cracked regions, maintaining partial percolation pathways and confirming the robustness of the conductive network. The role of the elastomeric PEO/PAA layers was further clarified by control experiments (Fig. S8), which demonstrated that both pristine PU rubber substrates and PEO/PAA-coated PU could accommodate strains well beyond 100% without visible cracks. This exceptional ductility explains why, within the QL films, the PEO/PAA bilayers act as compliant interlayers that absorb mechanical deformation, preventing premature fracture of the brittle TE BL systems.[55,56] By dissipating localized strain, they shield the rigid conjugated network from catastrophic failure, enabling the QL system to achieve a unique balance between TE functionality and stretchability.

The mechanical behavior of the constituent layers and the integrated QL composite was quantitatively assessed by AFM-based nanoindentation (Fig. S9). The pure PEO/PAA films displayed an extremely low elastic modulus of 30 MPa, consistent with their highly compliant and elastomeric nature. The PPyNPs/DWNT-PEDOT:PSS BL films exhibited a modulus of ~4.3 GPa, characteristic of rigid, densely packed nanoparticle-nanotube assemblies. Notably, the QL films presented an intermediate modulus (680 MPa) between these two extremes, which cannot be explained by a simple physical mixture. Rather, this intermediate value reflects effective stress transfer and strong interfacial coupling between the stiff PPyNPs/DWNT-PEDOT:PSS and the ductile PEO/PAA elastomer layers. Such behavior underscores that the QL architecture does not behave as a loosely stacked laminate of disparate layers; instead, it functions as a single integrated composite in which nanoscale interfaces govern the overall mechanics. This mechanical synergy enables the QL film to retain sufficient stiffness to maintain continuous conductive pathways while simultaneously offering the compliance required to accommodate large tensile strains.

3.6. TE response to tensile strain

Having demonstrated the superior mechanical compliance of the QL architecture, its TE performance under tensile strain was systematically investigated. At the unstrained state (0%), the 20 QL system displayed a lower PF (47.1 μW $m^{-1}K^{-2}$) compared with the pristine PPyNPs/DWNT-PEDOT:PSS BL films (183.3 μW m^{-1} K^{-2}), as shown in Fig. S10. This reduction is an expected trade-off arising from the incorporation of the electrically insulating PEO/PAA layers, which increased the overall film thickness (~2.55 μm for 20 QL cycles) and sheet resistance (~80 Ω sq^{-1} at 0% strain), thereby lowering both σ and S at the initial state. The strain-dependent TE response of the QL films is summarized in Fig. 8. The normalized resistance (R/R_0) remained stable up to 20% strain and showed only

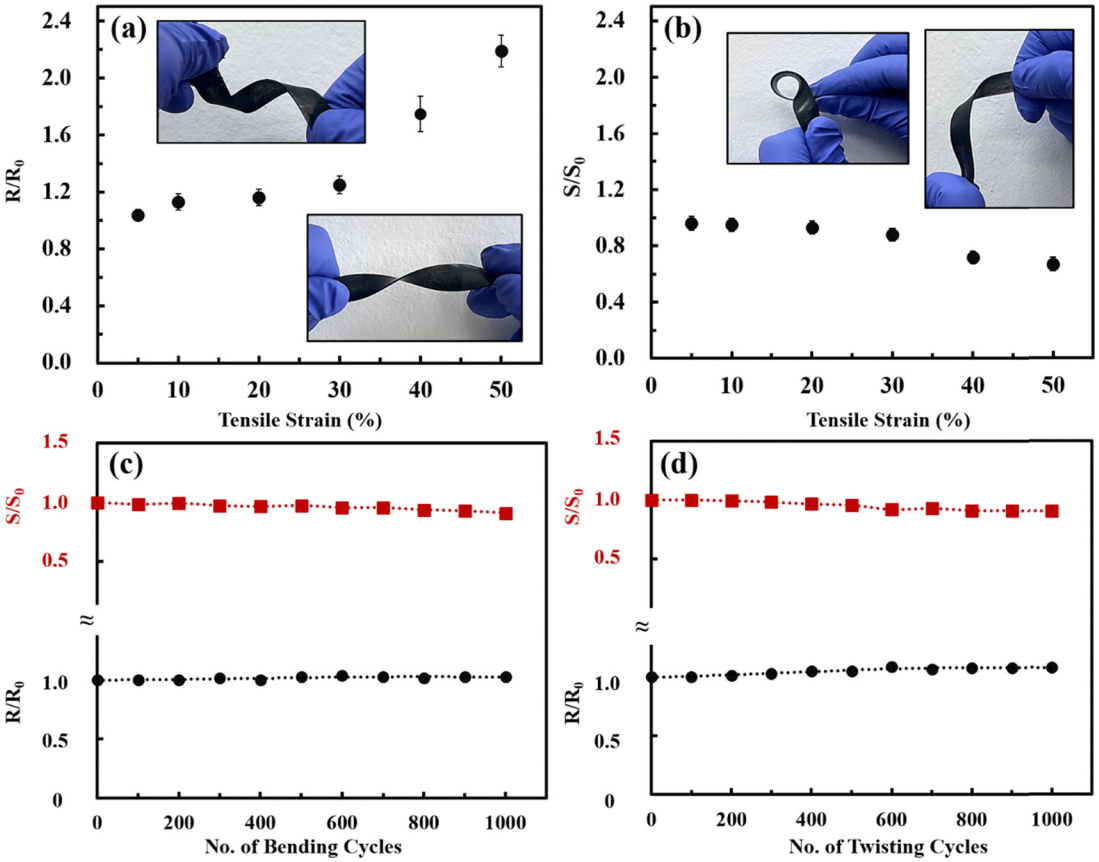

Fig. 8 Strain-dependent thermoelectric response of PPyNPs/DWNT-PEDOT:PSS/PEO/PAA QL films. (a) Normalized resistance (R/R_0) as a function of tensile strain, showing stable behavior up to ~30% strain and a sharp increase above 40%. (b) Normalized Seebeck coefficient (S/S_0) with strain, maintaining ~88% of its initial value at 30% strain but decreasing more significantly beyond 40%. (c) Normalized resistance and Seebeck coefficient after up to 1000 bending cycles with negligible degradation (<9%). (d) Normalized resistance and Seebeck coefficient after up to 1000 twisting cycles, showing less than 11% variation, confirming excellent durability under repeated deformation. Each inset photo shows the bending and twisting process.

a modest increase to ~1.25 at 30% strain (Fig. 8(a)). Such behavior is typical of percolated CNT-polymer networks, where elongation primarily increases tunneling distances between nanotube junctions without catastrophic network breakdown. Beyond 30% elongation, however, R/R_0 rose sharply, reaching ~2.19 at 50% strain, consistent with the initiation of cracks and partial disconnection of conductive pathways. Recent reports have demonstrated effective strategies to balance high TE performance and mechanical stretchability through microstructural composite design or ionic-liquid-mediated molecular modulation.[57,58] The present LbL-based architecture represents a structurally distinct approach, where nanoscale interfacial organization enables mechanical buffering without fundamentally altering the intrinsic conductive network.

The normalized Seebeck coefficient (S/S_0) exhibited complementary behavior (Fig. 8b). At 30% strain, S decreased by ~12% (from ~110 μV K^{-1} to ~97 μV K^{-1}), while further stretching to 50% strain led to a pronounced drop to $S/S_0 \approx 0.67$. Durability testing further demonstrated the mechanical compliance of the QL structure (Fig. 8c and d). After 1000 bending cycles with a tight radius of ~3 mm, the normalized resistance and S changed by less than 4% and 9%, respectively. Under twisting deformation, 1000 repeated cycles led to only ~8% resistance increase and ~11% reduction in S. The comparatively modest decrease in the S relative to the resistance change under applied strain suggests that the interfacial energy-filtering mechanism remains largely preserved during moderate deformation. While tensile strain increases the average tunneling distance between conductive junctions, leading to higher resistance, the nanoscale PPyNPs-DWNT-PEDOT:PSS interfaces responsible for energy-selective carrier transport remain locally intact up to ~30% strain, as confirmed by SEM analysis. Because the S is governed by the energy-dependent transport distribution near the Fermi level rather than purely by geometrical connectivity, the preservation of interfacial potential barriers maintains a relatively stable energy-filtering effect. Moreover, the elastomeric PEO/PAA interlayers dissipate mechanical stress and prevent interfacial delamination, thereby stabilizing the density-of-states gradient near E_F that governs thermopower generation. At larger tensile strains, progressive crack formation disrupts the electronic percolation pathways within the conjugated framework, resulting in a more pronounced decline in the S.

The integration of rigid TE systems (PPyNPs/DWNT-PEDOT:PSS) with ductile elastomeric layers (PEO/PAA) through LbL assembly provides a unique structural platform to resolve the

inherent conflict between electrical functionality and mechanical stretchability. The QL design enables a synergistic convergence of two otherwise antagonistic characteristics; high PF and large-strain deformability. Unlike conventional blending approaches, where rigid fillers disrupt the continuity of soft matrices or elastomers compromise conductive pathways, the nanoscale alternation achieved here yields a cooperative mechanical–electrical response in which each functional layer retains its intrinsic advantage while being reinforced by the complementary counterpart. The elastomeric PEO/PAA interlayers provide mechanical adaptability without sacrificing conduction pathways.[59] The compliant hydrogen-bonded elastomer layers dissipate applied stress, allowing the rigid conductive bilayers to undergo large deformation while preserving electrical continuity. Nanoindentation measurements further corroborate this synergy, with the QL films exhibiting an intermediate modulus that reflects strong interfacial coupling rather than a simple mixture of soft and rigid components. This mechanical accommodation is critical for maintaining stable TE performance under cyclic strain, as demonstrated by negligible degradation after 1000 bending and twisting cycles. The present work demonstrates that nanoscale architectural control *via* sequential assembly can integrate structurally dissimilar components into a mechanically unified yet electronically efficient material.

4 Conclusion

In summary, we demonstrated a rational LbL assembly approach for creating high-performance stretchable TE nanocomposites. Conductive PPyNPs/DWNT-PEDOT:PSS BL provided a 3D percolated network that achieved a PF of 183.3 $\mu W\ m^{-1}\ K^{-2}$, driven by enhanced carrier mobility and interfacial energy filtering. However, these brittle BL systems fractured at low strain ($\sim$5%). By introducing ductile PEO/PAA BL, we engineered a QL architecture that effectively dissipated mechanical stress while maintaining the integrity of the conjugated network. The QL films sustained tensile strains up to 30% without cracking, maintained $\sim$88% of S at this strain, and exhibited minimal degradation ($<$11%) in TE properties after 1000 bending and twisting cycles. This cooperative PPyNPs/DWNT-PEDOT:PSS/PEO/PAA architecture addresses the long-standing trade-off between electrical performance and stretchability in organic TE composites. The strategy presented here highlights nanoscale architectural control as a versatile platform for developing next-generation, eco-friendly TE power sources suitable for self-powered wearable electronics and IoT devices.

Conflicts of interest

The authors declare that they have no known competing financial interests or personal relationships that could have appeared to influence the work reported in this paper.

Data availability

The authors confirm that the data supporting the findings of this study are available within the article [and/or] its supplementary information (SI). Supplementary information is available. See DOI: https://doi.org/10.1039/d5tc04337a.

Acknowledgements

This work was supported by the National Research Foundation of Korea (NRF) grant funded by the Korea government (MSIT) (No. RS-2024-00405537). This research was also supported by the Institute of Information & Communications Technology Planning & Evaluation (IITP)-Innovative Human Resource Development for Local Intellectualization program grant funded by the Korea government (MSIT) (IITP-2026-RS-2024-00439292). Mario Culebras acknowledges the support received through the grant PID2024-160385OB-C21 funded by MICIU/AEI.

References

1 V. T. N. Linh, S. Han, E. Koh, S. Kim, H. S. Jung and J. Koo, *Biomaterial*, 2025, **314**, 122865.
2 M. Gao, Y. Yao, Y. Wang, B. Wang, P. Wang, Y. Wang, J. Dai, S. Liu, J. F. Torres and W. Cheng, *Nano Energy*, 2023, **107**, 108107.
3 S. E. Root, S. Savagatrup, A. D. Printz, D. Rodriquez and D. J. Lipomi, *Chem. Rev.*, 2017, **117**, 6467–6499.
4 T. R. Ray, J. Choi, A. J. Bandodkar, S. Krishnan, P. Gutruf, L. Tian, R. Ghaffari and J. A. Rogers, *Chem. Rev.*, 2019, **119**, 5461–5533.
5 A. Ali, H. Shaukat, S. Bibi, W. A. Altabey, M. Noori and S. A. Kouritem, *Energy Strat. Rev.*, 2023, **49**, 101124.
6 Q. Li, M. Gao, X. Sun, X. Wang, D. Chu, W. Cheng, Y. Xi and Y. Lu, *Mater. Sci. Eng. R Rep.*, 2025, **163**, 100934.
7 W. Tang, Q. Sun and Z. L. Wang, *Chem. Rev.*, 2023, **123**, 12105–12134.
8 P. Fernández-Yáñez, V. Romero, O. Armas and G. Cerretti, *Appl. Therm. Eng.*, 2021, **196**, 117291.
9 M. N. Hasan, H. Wahid, N. Nayan and M. S. Mohamed Ali, *Int. J. Energy Res.*, 2020, **44**, 6170–6222.
10 H. Han, L. Zhao, X. Wu, B. Zuo, S. Bian, T. Li, X. Liu, Y. Jiang, C. Chen and J. Bi, *J. Mater. Chem. A*, 2024, **12**, 24041–24083.
11 M. Martin-Gonzalez, K. Lohani and N. Neophytou, *Energy Mater.*, 2025, **5**, 500121.
12 H. Ming, Z.-Z. Luo, Z. Zou and M. G. Kanatzidis, *Chem. Rev.*, 2025, **125**, 3932–3975.
13 M. Channegowda, R. Mulla, Y. Nagaraj, S. Lokesh, S. Nayak, S. Mudhulu, C. K. Rastogi, C. W. Dunnill, H. K. Rajan and A. Khosla, *ACS Appl. Energy Mater.*, 2022, **5**, 7913–7943.
14 H. Jin, J. Li, J. Iocozzia, X. Zeng, P. C. Wei, C. Yang, N. Li, Z. Liu, J. H. He and T. Zhu, *Angew. Chem., Int. Ed.*, 2019, **58**, 15206–15226.

15 X.-L. Shi, N.-H. Li, M. Li and Z.-G. Chen, *Chem. Rev.*, 2025, **125**, 7525–7724.
16 B. Russ, A. Glaudell, J. J. Urban, M. L. Chabinyc and R. A. Segalman, *Nat. Rev. Mater.*, 2016, **1**, 1–14.
17 D. Zhou, H. Zhang, H. Zheng, Z. Xu, H. Xu, H. Guo, P. Li, Y. Tong, B. Hu and L. Chen, *Small*, 2022, **18**, 2200679.
18 J. S. Yun, S. Choi and S. H. Im, *Carbon Energy*, 2021, **3**, 667–708.
19 S. Zhou, X. L. Shi, L. Li, Q. Liu, B. Hu, W. Chen, C. Zhang, Q. Liu and Z. G. Chen, *Adv. Mater.*, 2025, **37**, 2500947.
20 T. A. Yemata, A. K. K. Kyaw, Y. Zheng, J. Xu, W. S. Chin, Q. Zhu and Y. Hayashi, *J. Mater. Chem. A*, 2025, **13**, 35976–35998.
21 R. Rubio-Govea, R. Félix, R. G. Wilks, M. Bär and K. A. Mazzio, *Adv. Electron. Mater.*, 2023, **9**, 2300076.
22 G. Calabrese, R. Cecchini, D. Gentili, D. Marini, M. Ferri, F. Mancarella, L. Barba, M. Cavallini, V. Morandi and F. Liscio, *ACS Nano*, 2024, **18**, 32781–32792.
23 Q. Jiang, J. Yang, P. Hing and H. Ye, *Mater. Adv.*, 2020, **1**, 1038–1054.
24 C. Cho, K. L. Wallace, P. Tzeng, J. H. Hsu, C. Yu and J. C. Grunlan, *Adv. Energy Mater.*, 2016, **6**, 1502168.
25 C. Cho, S. Qin, K. Choi and J. C. Grunlan, *ACS Appl. Polym. Mater.*, 2019, **1**, 1942–1947.
26 A. Hanif and D. S. Kim, *Adv. Sens. Res.*, 2025, **4**, 2400133.
27 C. Wang, K. Xia, H. Wang, X. Liang, Z. Yin and Y. Zhang, *Adv. Mater.*, 2019, **31**, 1801072.
28 C. Harito, D. V. Bavykin, B. Yuliarto, H. K. Dipojono and F. C. Walsh, *Nanoscale*, 2019, **11**, 4653–4682.
29 Y. Hao, X. He, L. Wang, X. Qin, G. Chen and J. Yu, *Adv. Funct. Mater.*, 2022, **32**, 2109790.
30 Y. Chang, Y.-H. Huang, P.-S. Lin, S.-H. Hong, S.-H. Tung and C.-L. Liu, *ACS Appl. Mater. Interfaces*, 2024, **16**, 3764–3777.
31 J. J. Richardson, J. Cui, M. Bjornmalm, J. A. Braunger, H. Ejima and F. Caruso, *Chem. Rev.*, 2016, **116**, 14828–14867.
32 P. V. Pham, H.-B. Do, M. Vasundhara, V.-H. Nguyen, T. Nguyen, H. Van Bui, V.-D. Dao, R. K. Gupta, V. K. Ponnusamy and J.-H. Park, *Chem. Soc. Rev.*, 2024, **53**, 190–5226.
33 Q. An, T. Huang and F. Shi, *Chem. Soc. Rev.*, 2018, **47**, 5061–5098.
34 X.-H. Shi, Y.-J. Xu, J.-W. Long, Q. Zhao, X.-M. Ding, L. Chen and Y.-Z. Wang, *Chem. Eng.*, 2018, **353**, 550–558.
35 L. Li, Q. Su, W. Xiao, J. Yan, H. Wu, J. Wang, Z. Liu, H. Li, H. Xue and L. Wang, *Composites, Part B*, 2025, **296**, 112235.
36 M. David, M. M. Barsan, C. M. Brett and M. Florescu, *Sens. Actuators, B*, 2018, **255**, 3227–3234.
37 Y. Zhang, L. Zhang, Z. Wang and G. Chen, *EnergyChem*, 2026, **8**, 100181.
38 M. Culebras, Y.-y Byun, J. Jang, T. K. Lee, D. Choi, A. Serafin, M. N. Collins, J. S. Cho and C. Cho, *ACS Appl. Energy Mater.*, 2024, **7**, 2351–2361.
39 B. S. Shim and N. A. Kotov, *Langmuir*, 2005, **21**, 9381–9385.
40 C. Cho, B. Stevens, J.-H. Hsu, R. Bureau, D. A. Hagen, O. Regev, C. Yu and J. C. Grunlan, *Adv. Mater.*, 2015, **27**, 2996–3001.
41 E. Detsri and S. T. Dubas, *Colloids Surf., A*, 2014, **444**, 89–94.
42 K. Choi, J. Son, Y. T. Park, J. S. Cho and C. Cho, *Macromol. Res.*, 2020, **28**, 997–1002.
43 G. M. Weng, J. Li, M. Alhabeb, C. Karpovich, H. Wang, J. Lipton, K. Maleski, J. Kong, E. Shaulsky and M. L. Elimelech, *Adv. Funct. Mater.*, 2018, **28**, 1803360.
44 T. Nakashima, J. Zhu, M. Qin, S. Ho and N. A. Kotov, *Nanoscale*, 2010, **2**, 2084–2090.
45 C. Xiao, Z. Li, K. Li, P. Huang and Y. Xie, *Acc. Chem. Res.*, 2014, **47**, 1287–1295.
46 H. Wang and C. Yu, *Joule*, 2019, **3**, 53–80.
47 A. C. Bhowal, H. Talukdar and S. Kundu, *Polym. Bull.*, 2019, **76**, 5233–5251.
48 A. Kahn, *Mater. Horiz.*, 2016, **3**, 7–10.
49 M. Jonson and G. Mahan, *Phys. Rev. B:Condens. Matter Mater. Phys.*, 1980, **21**, 4223.
50 D. Beretta, A. J. Barker, I. Maqueira-Albo, A. Calloni, G. Bussetti, G. Dell'Erba, A. Luzio, L. Duo, A. Petrozza and G. Lanzani, *ACS Appl. Mater. Interfaces*, 2017, **9**, 18151–18160.
51 S. Liu, H. Li, X. Fan and C. He, *Compos. Sci. Technol.*, 2022, **221**, 109347.
52 X. Fan, X. Zhang, X. Zhang, B.-C. Shiu, J.-H. Lin, C.-W. Lou and T.-T. Li, *Polymer*, 2023, **283**, 126224.
53 J. B. Gilbert, M. F. Rubner and R. E. Cohen, *Proc. Natl. Acad. Sci. U. S. A.*, 2013, **110**, 6651–6656.
54 C. Picart, J. Mutterer, L. Richert, Y. Luo, G. Prestwich, P. Schaaf, J.-C. Voegel and P. Lavalle, *Proc. Natl. Acad. Sci. U. S. A.*, 2002, **99**, 12531–12535.
55 F. Xiang, S. M. Ward, T. M. Givens and J. C. Grunlan, *ACS Macro Lett.*, 2014, **3**, 1055–1058.
56 S. G. Fisher, H.-C. Chiang, E. T. Iverson, E. Chang and J. C. Grunlan, *RSC Appl. Polym.*, 2024, **2**, 356–364.
57 Z. Li, L. Deng, H. Lv, L. Liang, W. Deng, Y. Zhang and G. Chen, *Adv. Funct. Mater.*, 2021, **31**, 2104836.
58 Y. Zhang, Y. Zhang, W. Deng, Q. Li, M. Guo and G. Chen, *Adv. Funct. Mater.*, 2025, **35**, 2420644.
59 C. Cho and J. O. Son, *Nanomaterial*, 2019, **10**, 41.

